Research Article | Vol. 29, No. 12 / 7 June 2021 / Optics Express 18932
Optics EXPRESS

Perforated extensible 3-D hyperbolic secant lens antenna for directive antenna applications using additive manufacturing

WENYI SHAO,* HIROYASU SATO, XIAOTONG LI, KEVIN KIPRUTO MUTAI, AND QIANG CHEN

Department of Communications Engineering, School of Engineering, Tohoku University, Sendai 980-8579, Japan
shao-w@ecei.tohoku.ac.jp

Abstract: In this paper, a novel three-dimensional (3-D) generalized hyperbolic secant (H-S) lens is first introduced using perforated dielectric material. The attractiveness of this new lens is its unique intrinsic flat shape characteristic and extensibility for different configuration scenarios, which provide a potential alternative design for a planar Luneburg and half Maxwell fish-eye lens based on a complex conformal mapping method. A high gain and wideband printed antipodal fermi antenna as a feeding source is employed in the proposed lens antenna prototype. The high radiation performance with low side lobe level of the fabricated lens prototype is validated from 8.2GHz to 12.5GHz, demonstrating 23.8 dBi realized gain at 10 GHz with 3-dB beamwidth of 9° and 2-dB fractional gain bandwidth of 41.6%. Besides, the total radiation efficiency is above ~40% across all tested frequencies, which suggests the proposed H-S lens itself has a broadband response. The simplicity and low-cost fabrication using additive manufacturing of its lens design indicates great potential in broadband high directive antenna applications.

1. Introduction

Lens antennas have been widely used for many applications at millimeter waves, like imaging systems [1], massive MIMO systems [2], wireless and satellite communication systems and radar systems [3], due to their simplicity, invulnerability to small imperfections, compact and flexible beam steering ability. Especially, the unprecedented demand in modern wireless communications systems, such as ever-higher data rate and capacity, motivates the development of highly directive antenna with low power consumption. The traditional methods to realize directive antenna are transmit-array antenna (TA) [4], reflect-array antenna (RA) [5] and dielectric lens antenna [6]. Although the beams with high directive and narrow main lobe can be generated, the TA requires masses of metallic phase-delaying elements with narrow band limitation that increase bandwidth reduction of TA. Several methods have been proposed over the years to improve the bandwidth of TA. But the complex design structure and overall cost of TA limits its application. Similar to the TA, RA is also an attractive and alternative way to produce high directive beams and efficiency due to its unique advantage of combing the features of reflectors and antenna arrays [7]. Nevertheless, the RA makes the overall systems vulnerable to interference due to the constraint on its physical dimensions and the feed blockage. Traditional dielectric lens antennas are a particularly useful approach for concentrating the radiated energy into a narrow beam in desired directions with more advantages such as high gain, low sidelobe level (SLL), broadband and good return loss. But they are usually cumbersome and high profile (e.g., spherical surface, parabolic surface) that poses a challenge for antenna system implementation.

Unlike the TA, RA and traditional dielectric lens antenna, planar dielectric gradient index (GRIN) lens antenna can overcome the drawbacks of narrow bandwidth, large loss inherent in electric or magnetic resonant metallic structure and bulky profiles. Moreover, it has the

#426824 https://doi.org/10.1364/OE.426824
Journal © 2021 Received 1 Apr 2021; revised 15 May 2021; accepted 22 May 2021; published 2 Jun 2021

Optics EXPRESS

advantages of compact, cost-effectiveness, reduced weight, competitive efficiency and ease of fabrication. The typical Luneburg lens is spherical symmetric GRIN lens, whose refractive index varies radially from the center to the outermost surface. It has excellent properties such as intrinsic broadband behavior and focusing beam from all directions equally well [8], which exhibits a narrow beam and multibeam capacity. Like Luneburg lens, the Maxwell fish-eye lens is another typical GRIN lens, which can transform a point source to a diametrically opposite focal point on the lens rim. In practical antenna application, half Maxwell fish-eye lens (HMFE) structure is proposed and utilized as a highly directive antenna [9]. But the manufacture of the constantly changing radial permittivity distribution of Luneburg and HMFE lens turns out to be challenging and complex. To eliminate the limitation of its spherical or hemispherical shape, a more convenient approach is to use transformation optics (TO) [10], quasi-conformal transformation optics (QCTO) [11] or field transformation [12] to form a planar Luneburg lens and hemispherical while maintaining the original electromagnetic performances. Convenient dielectric material structures such as air-holes and cube-shaped structures based on effective medium theory are utilized to achieve intended permittivity distribution by additive manufacturing or PCB milling techniques. Furthermore, the GRIN lens has been manufactured by metamaterials consisting of many sub-wavelength metallic resonant structures [13]. However, compared to porous dielectric structures, the inherent drawbacks of large loss and narrow bandwidth as well as complicated and expensive fabrication process exist. Other materials such as foam [14] and ceramic materials [15] are also utilized to generates the various permittivity values, which needs a complex and special process techniques.

Despite it having many advantages like the above-mentioned GRIN lens, a self-focusing cylindrical lens structure has not been exhaustively reported in the literature of microwave applications, thereafter known as hyperbolic secant (H-S) lens [16]. It is also called hyperbolic cosine lens or Mikaelian lens. The main difference of the H-S lens with respect to the Luneburg and HMFE lens is its intrinsic flat shape characteristic. It means the complex TO, QCTO or field transformation (FT) mapping methods is not required to flatten the particular shape (e.g., spherical shape) of lens. Moreover, the refractive index profile of H-S lens is the axial-symmetric, which makes it easier and quicker to manufacture. Because it is a more general form of quadratic index profiles (another GRIN index profile), the optimum structural size of H-S lens for integrated lens antenna and off-body fed lens antenna configurations could be easily determined by selecting the appropriate gradient parameter of H-S index profile, as shown in Fig. 1. Most importantly, all previous studies of H-S lens antenna mainly focus on the typical case with blocky structure in two-dimensional (2D) structure [14,17] that the source feed is placed on the lens surface as shown in Fig. 1(a).

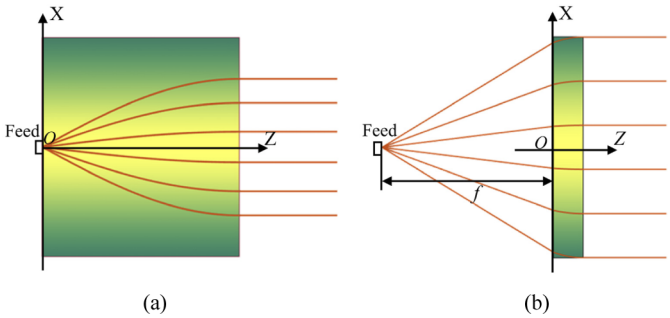

Fig. 1. The schematic diagram of the extensible characteristics of H-S lens. (a) Typical H-S lens for integrated lens antenna. (b) Generalized H-S lens for off-body fed lens antenna.

Optics EXPRESS

To the best of our knowledge, this paper first introduces a three-dimensional (3-D) generalized H-S lens antenna using perforated dielectric material based on effective medium theory. The proposed H-S lens is completely dielectric, and no metal are used to overcome the drawbacks of using inherently narrowband, lossy and dispersive [18] metamaterial with metallic resonators. Compared to a typical H-S lens, it's more flexible and extensible for high directive antenna application. Furthermore, a rapid prototyping, easily accessible and low-cost 3-D printing technique is utilized to fabricate the proposed lens prototype operating at 10GHz. By combing ray-tracing analysis and full-wave electromagnetic simulation in CST Microwave Studio, the focusing properties of generalized H-S lens are presented. Instead of conventional horn antenna, a printed antipodal fermi antenna (APFA) with corrugation structure is introduced as the source feed, providing the advantages of broad bandwidth, high gain, and lightweight. The high radiation performance with low side lobe level of 3-D generalized H-S lens antenna prototype is validated from 8.2GHz to 12.5GHz (X-band). Besides, its capability of beam-steering is explored with a preliminary study. This low-profile H-S lens could be a potential alternative design for planar Luneburg, HMFE or other GRIN lens to avoid using complex TO, QCTO or FT mapping methods.

2. Hyperbolic secant lens antenna design

2.1. Design theory of the hyperbolic secant lens

The H-S lens is a self-focusing cylindrical lens with unique characteristics that the rays oscillate in a sinusoidal way along the optical axis as shown in Fig. 2. Here, the oscillation period of the rays inside H-S lens is defined as pitch (p). Various characteristics of the rays such as focusing, diverging and collimation can be realized by choosing different pitches. Specially, when the incident rays are parallel to the optical axis with $p = 0.25$, it converges and focus at the rear surface of the H-S lens. If p<0.25, the parallel incident rays still can be focused, in which case the focal point appears at the outside of lens. This unique characteristic provides a potential way to design integrated lens antennas and off-body fed lens antenna by simply adjusting the pitch and thickness of H-S lens, as previously mentioned.

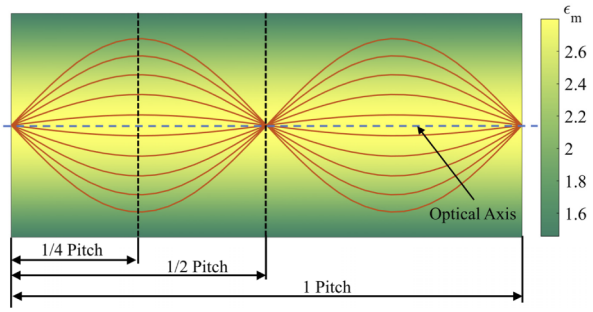

Fig. 2. The unique self-focusing properties of the H-S lens. The solid orange curve represents the trajectory of the rays. ε_m. represents the material permittivity.

It is well known that the ray tracing theory is a very useful tool to deal with the electromagnetic wave propagation in GRIN lens by the use of geometrical optics approximation. The ray behavior inside H-S lens can be also explained by Ray equation. This ray equation can be obtained from the expression of a differential arc length along a ray within lens. The transverse refractive index profile of H-S lens is defined by the following equation [16]

$$n(x) = n_0 \mathrm{sech}(\alpha x) \tag{1}$$

Optics EXPRESS

where n_0 is the central refractive index along the z-axis. $\alpha = 2\pi p/w$ is a gradient parameter. w is the thickness of lens. Figure 3(a) illustrates the ray trajectory through the H-S lens. The differential arc length can be mathematically expressed by the following equation.

$$ds = \sqrt{(dx)^2 + (dz)^2} \tag{2}$$

Here, we can define $\dot{x} = dx/dz$, then

$$ds = \sqrt{1 + (\dot{x})^2}dz \tag{3}$$

According to [19], the third optical direction cosine is invariant along any ray within lens, and defined as follows:

$$l_0 = n(x)\frac{dz}{ds} = \frac{n(x)}{\sqrt{1 + (\dot{x})^2}} \tag{4}$$

Equation (4) can be written as

$$dz = \frac{l_0}{\sqrt{n(x)^2 - {l_0}^2}}dx \tag{5}$$

Then, we can get the initial ray trajectory between any two points by substituting (1) into (5) and performing the integration with respect to x

$$z = \int_{x_0}^{x} \frac{l_0}{\sqrt{n(x)^2 - l_0^2}}dx = \int_{x_0}^{x} \frac{\cosh(\alpha x)}{\sqrt{A^2 - \sinh^2(\alpha x)}}dx \tag{6}$$

where A is a constant value and equals to $\sqrt{(n_0^2 - l_0^2)/l_0^2}$

Here, in order to solve Eq. (6), we use a transformation of the variables as defined below

$$u = \sinh(\alpha x) \tag{7}$$

Under this transformation, the ray trajectory between any two points within the H-S lens becomes

$$\begin{aligned} z &= \tfrac{1}{\alpha}\int_{u_0}^{u} \tfrac{1}{\sqrt{A^2-u^2}}dx \\ &= \tfrac{1}{\alpha}\left(\sin^{-1}\left(\tfrac{u}{A}\right) - \sin^{-1}\left(\tfrac{u_0}{A}\right)\right) \end{aligned} \tag{8}$$

where u_0 is the value of u at $z = 0$,that is $u_0 = \sinh(\alpha x_0)$.

Equation (8) can be written as

$$\alpha z + \sin^{-1}\left(\frac{u_0}{A}\right) = \sin^{-1}\left(\frac{u}{A}\right) \tag{9}$$

Here, we can define $\tau = \alpha z + \sin^{-1}(u_0/A)$,then

$$u(z) = A\sin(\tau) \tag{10}$$

Equation (10) indicates the ray position at each point within the H-S lens. The ray slope in the new u-z coordinate system can be calculated as follows:

$$\begin{aligned} \dot{u}(z) &= A\cos(\tau)\dot{\tau}(z) \\ &= A\cos(\tau)(\alpha z + \sin^{-1}(u_0/A))' = A\alpha\cos(\tau) \end{aligned} \tag{11}$$

After constituting the parameter to (10) and (11), and performing trigonometric manipulation, we can get the ray position and slope respectively.

Optics EXPRESS

The ray position:

$$u(z) = A\cos(\sin^{-1}(u_0/A))\sin(\alpha z) + u_0\cos(\alpha z) \tag{12}$$

The ray slope:

$$\dot{u}(z) = A\alpha(\cos\alpha z \cdot \cos(\sin^{-1}(u_0/A)) - (u_0/A)\sin(\alpha z)) \tag{13}$$

But

$$\cos(\sin^{-1}(u_0/A)) = \cos(\tau_0) = \dot{u}_0/(\alpha A) \tag{14}$$

where $\dot{u}_0$ and τ_0 are the values of $\dot{u}$ and τ at $z = 0$, respectively.

Then, substituting (14) into (12) and (13) respectively,

$$u(z) = u_0\cos(\alpha z) + \dot{u}_0\frac{\sin(\alpha z)}{\alpha} \tag{15}$$

$$\dot{u}(z) = -u_0\alpha\sin(\alpha z) + \dot{u}_0\cos(\alpha z) \tag{16}$$

we can obtain 2-by-2 ray transfer matrices to describe ray propagation in H-S lens,

$$\begin{pmatrix} u(z) \\ \dot{u}(z) \end{pmatrix} = \begin{pmatrix} \cos(\alpha z) & \frac{\sin(\alpha z)}{\alpha} \\ -\alpha\sin(\alpha z) & \cos(\alpha z) \end{pmatrix}\begin{pmatrix} u_0 \\ \dot{u}_0 \end{pmatrix} \tag{17}$$

After propagating through the H-S lens, the ray refracts obeying Snell's law and enters the free space as shown in in Fig. 3(a). The refracted rays finally intersect at a point. The distance between that point and rear surface of the H-S lens is defined as the back focal length f.

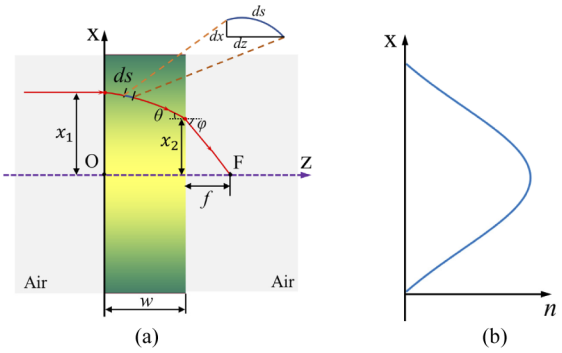

Fig. 3. (a). The schematic view of ray trajectory through the H-S lens. (b). Hyperbolic secant distribution of the refractive index (n) profile.

In order to calculate f, the Snell's law is applied at the rear surface of the H-S lens.

$$n(x_2)\sin\theta = n_{air}\sin\varphi \tag{18}$$

where $n(x_2) = n_0\text{sech}(\alpha x_2)$ and $n_{air} = 1$.

Optics EXPRESS

Here, the ray incident on H-S lens parallel to its optical axis (z-axis). $\theta = \tan^{-1}[\dot{u}(w)]$, then Eq. (18) can be written as follows

$$n_0 \mathrm{sech}(\alpha x_2)\sin\{\tan^{-1}[\dot{u}(w)]\} = \sin\varphi \tag{19}$$

That also means

$$\varphi = \sin^{-1}\left(n_0 \mathrm{sech}(\alpha x_2)\dot{u}(w)/\sqrt{\dot{u}(w)^2+1}\right) \tag{20}$$

From Fig. 3(a), the tangent of refracted angle φ can be determined as follows

$$\tan\varphi = \frac{x_2}{f} \tag{21}$$

Combine Eqs. (18), (19), (20) and (21) gives

$$f = \frac{x_2}{\tan\left\{\sin^{-1}\left[n_0 \mathrm{sech}(\alpha x_2)\dot{u}(w)/\sqrt{\dot{u}(w)^2+1}\right]\right\}} \tag{22}$$

According to the equation $\sin(\arctan(\upsilon)) = \upsilon/\sqrt{\upsilon^2+1}$, Eq. (22) can be also written as

$$f = \frac{x_2}{\tan\{\sin^{-1}[n_0 \mathrm{sech}(\alpha x_2)\sin(\tan^{-1}[\dot{u}(w)])]\}} \tag{23}$$

Under the paraxial approximation [20], that is $\theta \approx \tan\theta \approx \sin\theta$, the (23) can be further simplified as follows,

$$f = \frac{x_2}{n_0 \mathrm{sech}(\alpha x_2)\sin(\tan^{-1}[\dot{u}(w)])} = \frac{x_2}{n_0\dot{u}(w)} \tag{24}$$

Combine Eqs. (15), (16) and (24) gives

$$f = \frac{x_1\cos(\alpha w)}{n_0 \cdot |-x_1\alpha\sin(\alpha w)|} = = \frac{w}{2\pi p n_0}\cot(2\pi p) \tag{25}$$

Equation (25) provides a flexible and extensible dimension constraint for deigning H-S lens ($n_0 = 1.673$) as illustrated in Fig. 4. The pitch is easily tunable to get suitable lens width and back focal length. In a particular case, if pitch $p = 0.25$, the back focal length is equal to zero that means the focal point appears at the rear surface of the H-S lens as mentioned above.

2.2. Realization of the H-S lens profile with perforated structure

The perforation structure, traditionally, is achieved by drilling holes of various sizes in a dielectric material or additive manufacturing. The unit-cell element is a cube with circular air-hole, as shown in Fig. 5. The size of unit-cell element is $a = 7\ mm$, and P is the radius of circular air-hole. The unit-cell element can be easily and economically fabricated by using the additive manufacturing or 3D-printing.

Based on the effective medium theory, the equivalent effective relative permittivity (ε_e) of the unit-cell element can be controlled by changing the diameter of air-hole. Therefore, under the condition that the wave vector is perpendicular to the axis of air hole, ε_e can be calculated using the following expression [21].

$$\varepsilon_e = \frac{(a^2 - \pi P^2)\varepsilon_m + \pi P^2\varepsilon_{air}}{a^2} \tag{26}$$

where ε_{air} stands for the air permittivity. ε_m is the material permittivity. In our case, polylactic acid (PLA) plastic material is utilized to construct the H-S lens. It is one of the most commonly

Optics EXPRESS

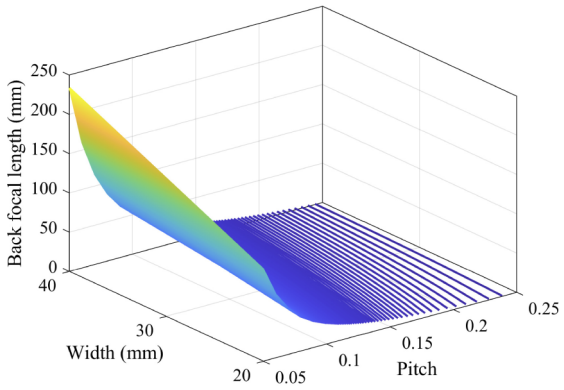

Fig. 4. 3D contour for dimension constraints of H-S Lens design.

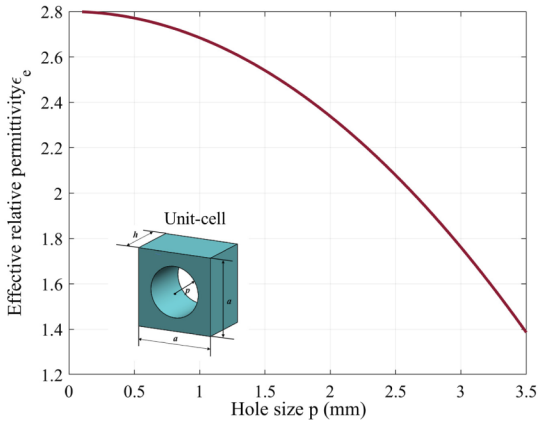

Fig. 5. Illustration of effective permittivity of unit-cell element with different hole size for PLA plastic materials.

used materials for 3D printing, which has a relative dielectric constant $\varepsilon_m \approx 2.75$, and loss tangent $\tan\delta \approx 0.011$ at 10 GHz [22]. For the special case that the whole region of the unit-cell element is occupied with air ($a = 2P$), the lowest achievable effective relative permittivity by using circular air-hole is 1.39.

The implemented design procedure of 3-D H-S lens designed to operate at 10 GHz is shown in Fig. 6. In this paper, the pitch, diameter, thick and back focal length of designed H-S lens is 0.05, 189mm, 35mm and 204.9 mm respectively. The continuous relative permittivity profile of H-S lens as shown in Fig. 6(a) need to be discretized into different layers (27 layers in this paper) by staircase approximation. Figure 6(b) and (c) illustrates the achieved 2-D continuous and discrete relative permittivity distribution respectively. The different sizes of perforation are utilized to obtain the discrete relative permittivity distribution as shown in Fig. 6(d). Table 1 lists the specific designed perforation sizes with each layer. Noted that only half of layer is shown owing to the axial symmetry of relative permittivity distribution of H-S lens.

In order to create the 3-D H-S lens, the discrete 2-D distribution need to be rotated around the central axis. Here, the cross-section of 3-D H-S lens model by rotating operation is shown in Fig. 7, which has circular geometry with the diameter of 189 mm and the thickness of 35mm. The designed back focal length is 204.9mm, and the back focal length to lens diameter ratio (f/D) is 1.08.

Optics EXPRESS

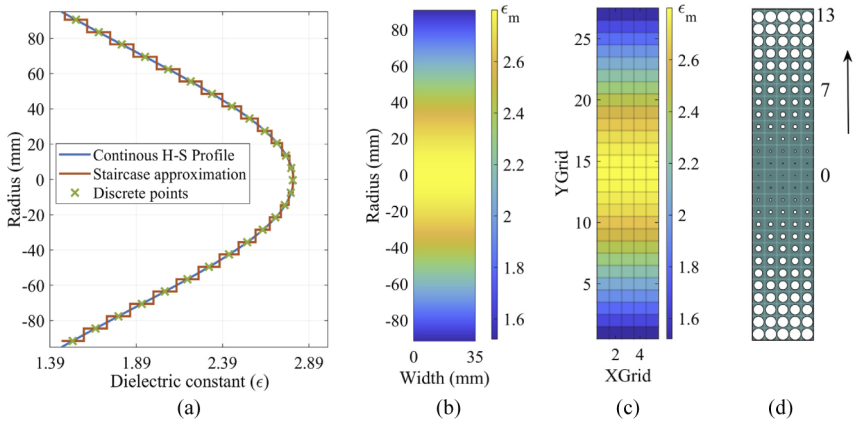

Fig. 6. The implemented design procedure of 3-D H-S lens designed to operate at 10 GHz. (a) Staircase approximation of continuous relative permittivity profile of H-S lens. (b) Continuous 2-D relative permittivity distribution. (c) Discrete 2-D relative permittivity profile. (d) Perforated dielectric structure of H-S lens.

Table 1. Designed Perforation Sizes with Each Layer

Layer	Diameter (mm)
0	0.316
1	0.653
2	1.226
3	1.816
4	2.399
5	2.968
6	3.517
7	4.042
8	4.542
9	5.013
10	5.456
11	5.870
12	6.253
13	6.608

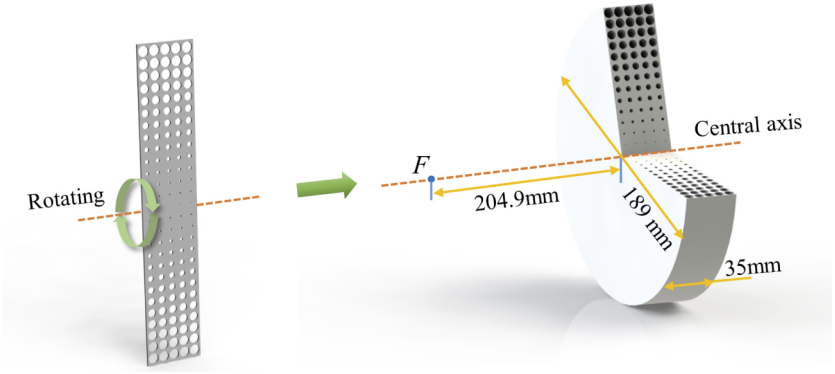

Fig. 7. Schematic of the cross-section of designed 3-D H-S lens model by rotating operation.

Optics EXPRESS

2.3. Focusing performances

To illustrate the H-S lens operation performance, a ray-tracing algorithm based on above-mentioned ray transfer matrices is applied to this relative permittivity distribution, launching rays from focal point that becomes parallel to the central axis, as shown in Fig. 8(c). The vertical dot line represents the focal plane. Besides, based on the electromagnetic field full-wave simulation, the 2-D electric field distribution, propagating through the lens is presented in Fig. 8(a) for WR-90 waveguide is placed at the focal point of H-S lens as a feed source. As expected, very good focusing properties are achieved that H-S lens can be a good phase transformer to convert a spherical wave into a plane wave. Figure 8(b), (d) illustrates the aperture phase and magnitude distribution at a plane which is located at the exit aperture of the H-S lens respectively. The phase uniformity across the actual physical aperture of the H-S lens is another evidence of the transformation of the spherical wave into plane wave. The magnitude of the E-field at the center of H-S lens is larger than that at the edge. The dot white and black circle represents the actual physical aperture of H-S lens (0.189m). It should be noted that the feed source does not need to be located at the surface of the lens, unlike the case of the typical H-S lens. Obviously, the results of these two approaches are in reasonable agreement, which indicates that the ray tracing method can be quite accurate for the analysis of H-S lenses.

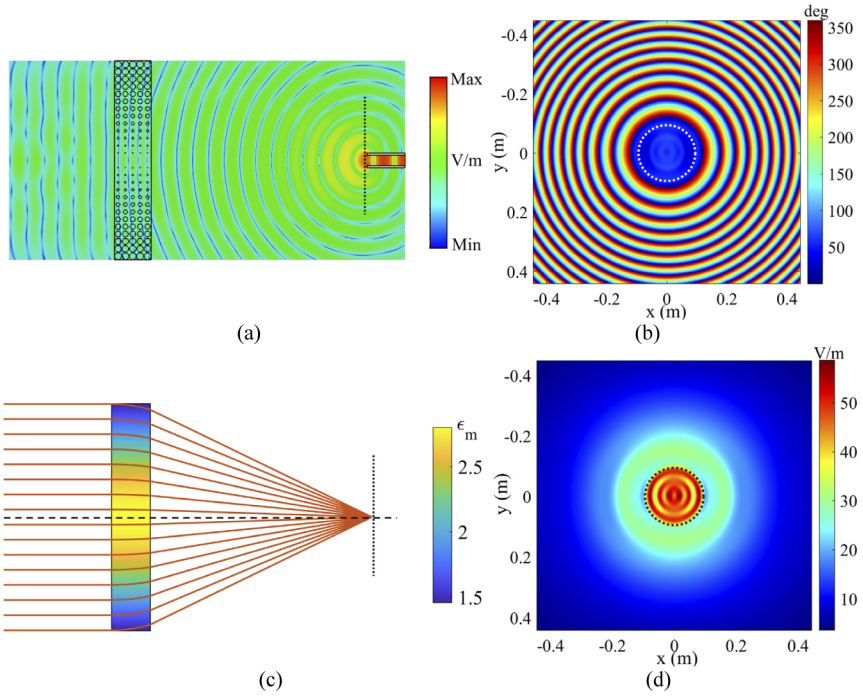

Fig. 8. Focusing performances of proposed H-S lens. (a) Simulated 2-D electric field distribution with WR-90 waveguide as source feed, and (b) The aperture phase distribution. (c). Ray tracing across the H-S lens. The vertical dot line is the focal plane. (d) The aperture amplitude distribution. Noted that the dot white and black circle represents the actual physical aperture (0.189 m diameter) of H-S lens.

2.4. Lens feeding structure design

Common requirements for a feed source of lens are low back-to-front radiation ratio, minimum spillover losses, well-defined phase center coincident with the focal point and effective illumination.

Optics EXPRESS

Conventionally, patch antenna, slot antenna, horn antenna and waveguide are commonly utilized as feed sources. Unlike the case of resonant metamaterials lens that are inherently narrowband, the intrinsic broadband response of dielectric lens is usually limited by the bandwidth of the feed source [15]. In our case, to realize the broadband lens antenna, a printed antipodal fermi antenna (APFA) with corrugation structure [23] is designed with advantages of broad bandwidth, high gain, and lightweight. The schematic of APFA structure is shown in Fig. 9. One pair of antipodal Femi-Dirac type tapered slot is etched on the on both sides of dielectric substrate with a relative permittivity of 3.3, loss tangent 0.001 and a thickness of 0.8 mm. The curve of Femi-Dirac type tapered slot is determined by

$$f_{APFA}(z) = \frac{-a_s}{1 + e^{-b(z-c)}} \tag{27}$$

where a_s is the asymptotic value of the width of the taper for $z \to \infty$. b is related to the gradient at inflection point.c denotes the position of inflection point of Fermi-Dirac function.

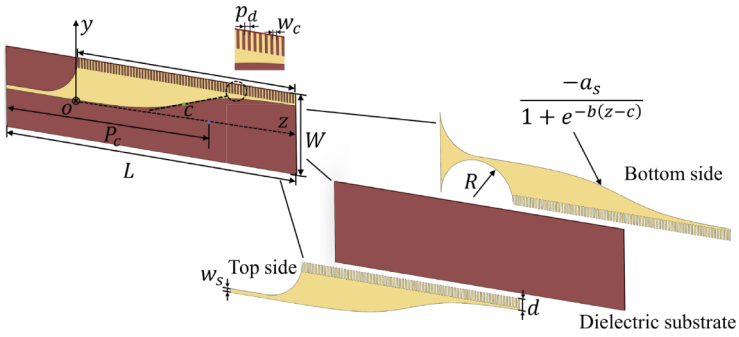

Fig. 9. The schematic of APFA structure at 10 GHz. One pair of antipodal Femi-Dirac type tapered slot is etched on the on both sides of dielectric substrate.

In our case, the specific design parameters of APFA are list in Table 2. The typical characteristic of APFA is the rectangular corrugations on the lateral side of the substrate, which can enlarge the effective aperture and guarantee the same phase inside and outside the tapered slot. And for that, this corrugation structure is very useful to reduce the side lobe levels and increase the gain.

Table 2. Geometry Dimensions of APFA Structure

Dimensions	Values
L	160 mm
W	42mm
P_c	110mm
R	20mm
d	6mm
ws	2mm
p_d	1.6mm
wc	0.8mm
a_s	15
b	0.08
c	60

The performance characteristics of the APFA are shown in Fig. 10. The E-plane and H-plane is defined as y-z and x-z plane, respectively. Figure 10(a) and (b) illustrates the simulated and

Optics EXPRESS

measured normalized radiation patterns for the APFA, for both E-plane and H-plane. Good agreement between simulated and measured radiation patterns (Co-Pol radiation) is obtained with a peak realized gain of 14.2 dBi. Besides, the side lobe level (SLL) is lower than ~17 dB for both E-plane and H-plane. The measured reflection coefficient S11 of the APFA are shown in Fig. 10(c). It can be observed that the measured S11 are almost less than -10 dB from 8.2 GHz to 12.5GHz. Figure 10(d) shows there are some differences between measurement and simulated results about 1-2 dB in the frequency region of 8.2-12.5GHz. The phase center is an approximate point in space that need to be coincident with the lens focal point to minimize phase error over aperture. Here, the approximate phase center location of APFA is at $P = 110mm$ with frequency 10GHz.

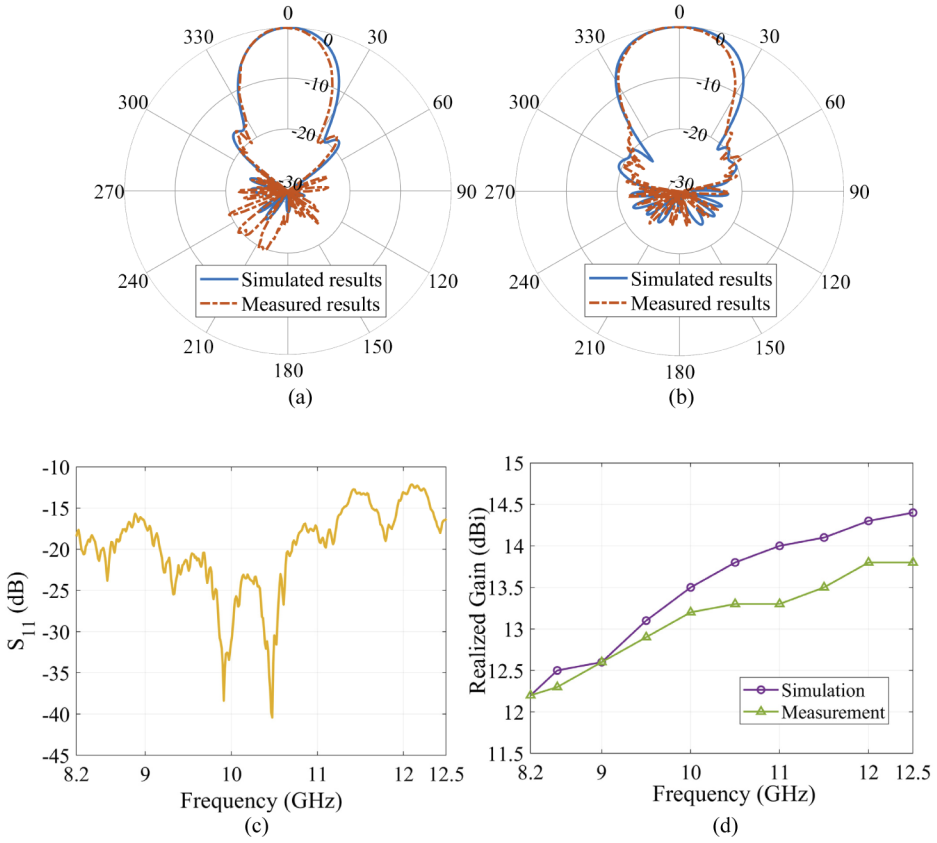

Fig. 10. APFA performance. (a), (b) Measured and simulated E- and H-plane normalized radiation patterns at 10 GHz. (c) Measured reflection coefficient S11 of APFA. (d) Measured and simulated Realized gain.

3. Numerical verification, fabrication and measurement results

3.1. Modeling and simulation results

To validate the design, the proposed 3-D H-S lens antenna model is constructed and simulated using the electromagnetic field full-wave simulation in CST Microwave Studio. Figure 11 illustrates the schematic 3D view of the designed H-S lens antenna system. It consists of three main parts, the H-S lens, its feeding source (APFA) and the supporting foam. It is noted that the phase center of APFA varies based on the frequency. There is some variation (10~20mm)

Optics EXPRESS

in approximate phase center location from 8.2 GHz to 12.5 GHz. The phase center should be located at the focal point of H-S lens to obtain an optimum coupling. As mentioned above, the approximate phase center location is at $P_c = 110mm$. with frequency 10GHz. So, the approximate distance (S) between APFA and H-S lens is 154.92 mm, which gives a −10 dB edge taper at the angle of 24.7 degree.

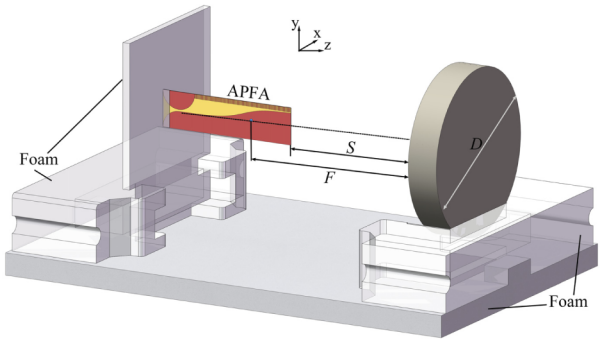

Fig. 11. 3-D perspective view of proposed H-S lens antenna system at 10 GHz composed of feeding source (APFA), H-S lens and the supporting foam.

Figure 12(a) and (b) illustrates the simulated radiation patterns for both Co- and Cross-polar in the E- and H-plane at 10 GHz respectively. The simulated realized gain of the H-S lens antenna is 24.7 dBi, which is 10.5 dBi higher than the feeding source of APFA itself. It also verifies that the excellent focusing feature of the H-S lens that effectively convert a spherical wave emitted by the feeding source to the approximate plane wave. Thus, the high realized gain is achieved owing to the phase delay introduced bthe dielectric perforation structure. Meanwhile, the cross-polar radiation patterns of both E- and H-plane show the cross-polarization level is very low, and is less than 25 dB. Figure 12(c) shows the simulated realized gain and the side lobe levels for different frequencies. The ~3-dB fractional realized gain bandwidth is 43.9% from 8 to 12.5 GHz, indicating the intrinsic broadband response of H-S lens. The side lobe levels remain lower than -14 dB across the frequency band of 8-12.5 GHz. To further assess the focusing feature of the lens, the aperture phase distribution at a plane which is located at the exit aperture of the H-S lens is respectively given in Fig. 12(d). As expected, the phase is uniform across the exit aperture plane of the H-S lens, which further demonstrate the high realized gain owing to the phase transformation function (spherical wave to plane wave) of the H-S lens.

3.2. Prototype fabrications

The 3-D printed planar H-S lens is built based on the fused deposition modeling (FDM) that is an additive manufacturing process. In FDM 3-D printer, the H-S lens model is constructed layer by layer by heating and extruding thermoplastic polymers in a filament form in a pre-determined path. Figure 13 shows the fabricated prototype of the proposed dielectric H-S lens, which is obtained by polylactic acid (PLA) plastic material.

In our case, the dimensional accuracy of the FDM 3D printer is quite limited, which requires the minimum wall thickness of ~0.8 mm. In order to prevent printed lens models from falling apart, we add the very thin supporting layer structures around the lens. It should be noted that the actual overall dimensions of the designed H-S lens are 191 × 191 × 36 mm, which is slightly larger than simulated one.

Optics EXPRESS

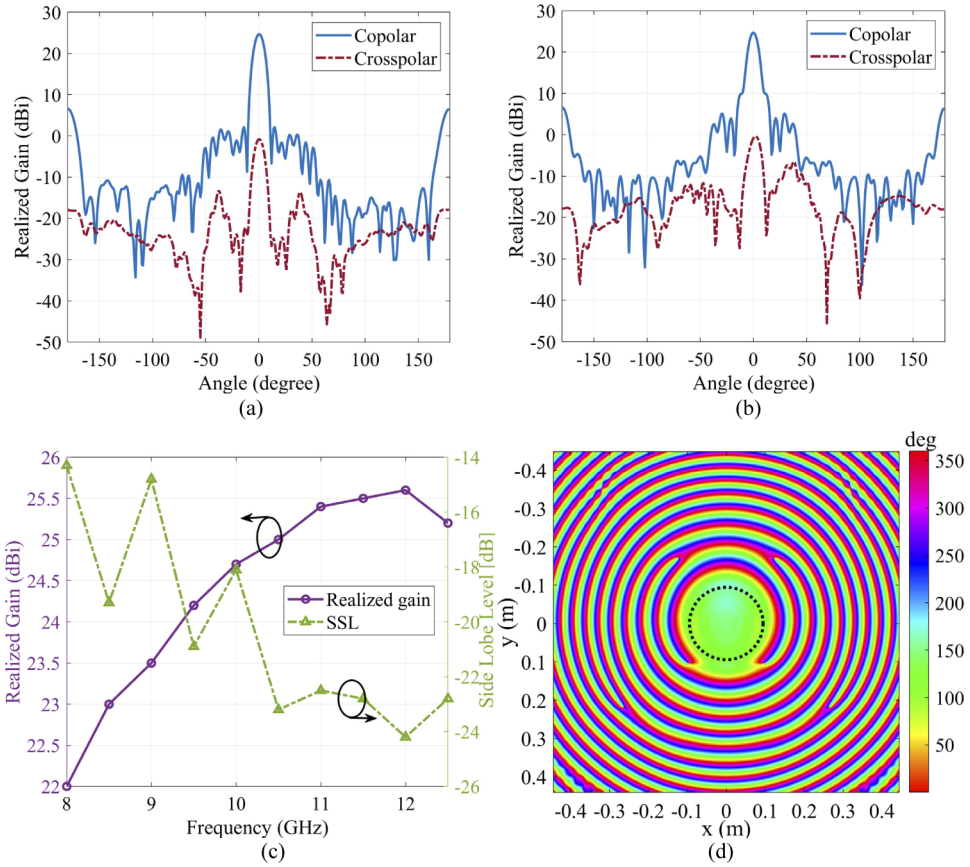

Fig. 12. Simulated co- and cross-polar radiation patterns in E-plane and H-plane respectively at 10 GHz. (a) E-plane. (b) H-plane. (c) Realized gain and Side lobe level. (d) The aperture phase distribution at a plane which is located at the exit aperture of the H-S lens. Noted that the black dot circle represents the actual physical aperture (0.189 m diameter) of H-S lens.

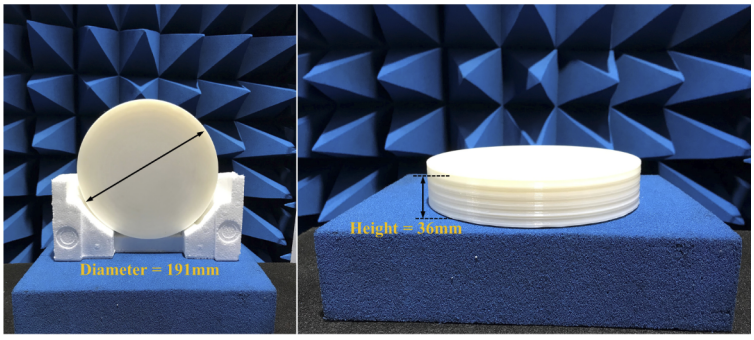

Fig. 13. Photograph of the fabricated prototype of the proposed H-S lens of 191 mm diameter and 36 mm height.

Optics EXPRESS

3.3. Experimental results and discussion

Here, a low-loss and lightweight foam-based structure is designed to support the H-S lens and APFA. Although an approximation distance between H-S lens and APFA has been given in section 3.1, it still needs to be adjusted to obtain the optimal value. The whole of the H-S lens antenna is used as the transmitting antenna and is placed on a rotating platform, as shown in Fig. 14. The measurement process is performed inside a far-field anechoic chamber using the gain transfer method and the Flann standard gain horn at X-band (Model 16240-20). Both the H-S lens antenna and horn antenna is connected to the Anritsu MS46322B vector network analyzer. By using the control application under LabVIEW environment, automatic measurements are carried out to characterize the H-S lens antenna performance from 8.2 to 12.5 GHz.

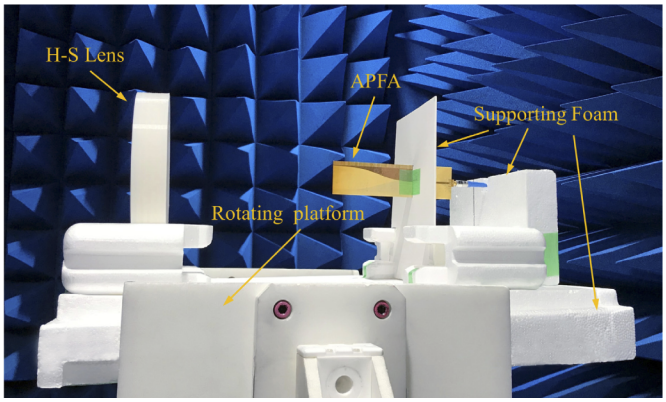

Fig. 14. Photograph of lens measurement setup in anechoic chamber.

Figure 15 illustrates the simulated and measured radiation patterns for both the Co-Pol and Cr-Pol in E-plane and H-plane respectively at 10 GHz. In general, there is a good consistency between the simulation and measurement results in terms of realized gain, side lobe levels and 3-dB beamwidth as shown in Table 3, which validates the discretization process of H-S lens. The measured sidelobe levels are −17.4 and −16.7 dB, and the 3-dB beamwidths are the same (9 degree) for the E-plane and H-plane, respectively. Furthermore, the measured cross-polar levels of both E- and H-plane still remains at a low level (<-21 dB). Owing to the accuracy of additive manufacturing and the limit of antenna measurement condition, there are also some differences between the simulated and measured results as shown in Fig. 15.

Table 3. Simulated and Measured Radiation Patterns Characteristic of H-S Lens at 10GHz

		Simulated	Measured
Realized Gain (dBi)		24.7	23.8
3-dB Beamwidth (°)	E-plane	9.2	9
	H-plane	8.7	9
Cr-pol Levels (dB)	E-plane	-25.5	-29.7
	H-plane	-25.1	-21.0
Side Lobe Levels (dB)	E-plane	-18.1	-17.4
	H-plane	-18.0	-16.7

Optics EXPRESS

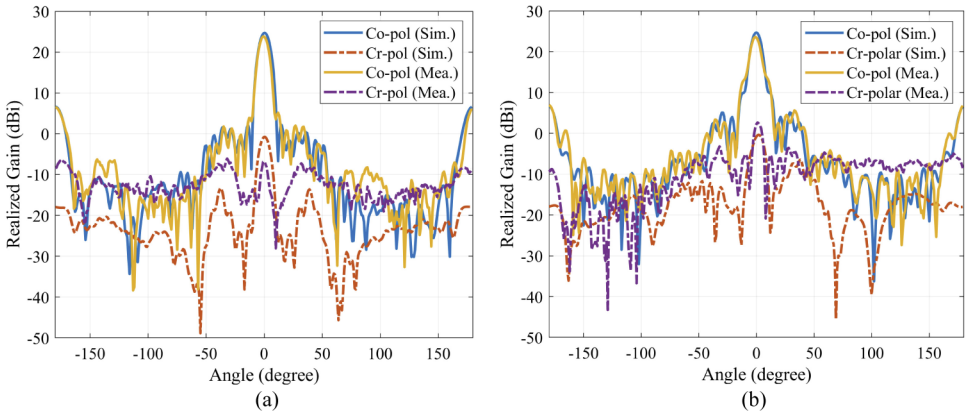

Fig. 15. Simulated and measured radiation patterns of the proposed H-S lens antenna at 10 GHz. (a) E-plane. (b) H-plane.

Another important parameter that measures the lens performance is the total radiation efficiency which is defined as follows [24]:

$$\eta = \eta_{ape} \cdot \eta_{rad} \tag{28}$$

where $\eta_{ape} = D_a\lambda^2/(4\pi A)$ is the aperture efficiency, D_a is the directivity of antenna, A is the physical aperture area of the lens and λ is the wavelength at the designed frequency. $\eta_{rad} = G_e/D_a$ is the radiation efficiency.G_e is the measured gain. Then the total radiation efficiency can be re-written as follows

$$\eta = G_e\lambda^2/(4\pi A) \tag{29}$$

The simulated overall antenna efficiency is 75.3%, which corresponds to a 24.7dBi gain. In our case, the measured gain is 23.8dBi. Considering the thin supporting layer structures added around lens, the actual physical aperture area is a little larger than that in simulation. The measured overall antenna efficiency is 59.9%. The experimental and simulated realized gain and their corresponding total radiation efficiencies in the frequency range of 8.2-12.5GHz are presented in Fig. 16, respectively. The measured 2-dB fractional realized gain bandwidth is 41.6% from 8.2 to 12.5GHz. The total radiation efficiency of H-S lens is above ~40% in the frequency range, and decreases as the frequency gradually increases. This shows that the proposed H-S lens itself has intrinsic broadband response.

Here, it should be noted that the total radiation efficiency is consider to be the aperture efficiency in some Refs. [25], or the total radiation efficiency values are not given directly [26–30]. Thus, the actual of total radiation efficiency lens cannot be fairly compared. Here, we re-calculate it based on the measured gain and physical aperture area presented in their papers. A brief comparison of our proposed H-S lens antenna with other designs published in the literature is given in Table 4.

Optics EXPRESS

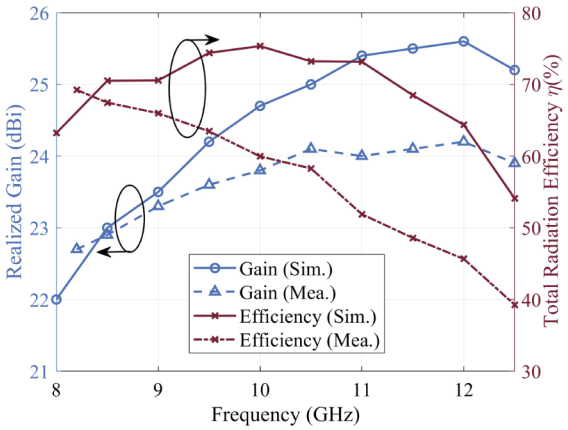

Fig. 16. Simulated and experimental realized gain and corresponding total radiation efficiency of the H-S lens antenna.

Table 4. Comparison between the Proposed H-S Lens Antenna and Previous Works

Ref.	η [%]	Gain [dBi]	Aperture area [λ^2]	Frequency [GHz]	F/D	T/D	Design style	Manufacture
[This work]	59.9	23.8	31.8	10	1.07	0.19	Flat circular GRIN	3-D Printing
[26]	27.4,19.1	18.3,18.9	19.6,32.3	60,77	0.25	0.28	Flat circular GRIN	3-D Printing
[27]	43.5	28.9	141.0	13.4	0.67	-	Curved GRIN	3-D Printing
[28]	40.9	32.5	346.3	42	0.40	0.08	Flat circular GRIN	3-D Printing
[31]	30.7	32.7	483.1	60	0.22	-	Flat circular Fresnel-zone	3-D Printing
[25]	72-31	29-34	0.89-576.5	14-40	0.63	0.16	Flat circular GRIN	PCB milling
[24]	67.3	22.2	19.6	13.4	0.60	0.22	Flat circular GRIN	PCB milling
[29]	36.7-62.6	19.8-24.3	-	13-18	-	-	Hemispherical GRIN	PCB milling
[32]	~60	~18	-	57-66	-	0.05	Flat circular GRIN	Foam pressing
[30]	50.5,40.5	17.3,24	8.4,49.2	8.2,19.8	-	-	Cubic GRIN	polymer jetting rapid prototyping

Optics EXPRESS

4. Conclusions

This article introduced a novel 3-D Extensible H-S Lens Antenna for high directive antenna application based on ray tracing analysis and full-wave electromagnetic simulation. The attractiveness of this new lens is its intrinsic flat shape characteristic and extensibility for different antenna application scenarios, in addition to the advantages of low-profile, lightweight, and high performance. The perforated dielectric material of variable hole sizes is utilized to satisfy the required H-S refractive index distribution. A high gain and wideband printed antipodal fermi antenna as feeding source is employed in the proposed lens antenna prototype operating at 10 GHz. The simulated and experimental results showed good agreement, demonstrating 23.8 dBi realized gain at 10 GHz with 3-dB beamwidth of 9o and 2-dB fractional realized gain bandwidth of 41.6%. Besides, the total radiation efficiency is above ~40% across all tested frequencies (8.2GHz-12.5GHz), which suggests the proposed H-S lens itself has intrinsic broadband response. A small steering angle of 14° is attained in the proposed lens design in this paper, however, it does not mean that higher steering angles cannot be obtained. The capability of beam steering is mainly limited by the physical size of H-S lens itself, focal length and feeding source design. Besides, the simplicity and low-cost fabrication of its lens design indicating great potentials in broadband high directive antenna applications.

Disclosures. The authors declare no conflicts of interest.

Data availability. Data underlying the results presented in this paper are not publicly available at this time but may be obtained from the authors upon reasonable request.

References

1. S. Yeom, D.-S. Lee, Y. Jang, M.-K. Lee, and S.-W. Jung, "Real-time concealed-object detection and recognition with passive millimeter wave imaging," Opt. Express **20**(9), 9371–9381 (2012).
2. X. Gao, L. Dai, S. Han, I Chin-Lin, and X Wang, "Reliable Beamspace Channel Estimation for Millimeter-Wave Massive MIMO Systems with Lens Antenna Array," IEEE Trans. Wireless Commun. **16**(9), 6010–6021 (2017).
3. J. R. Costa, C. A. Fernandes, G. Godi, R. Sauleau, L. Le Coq, and H. Legay, "Compact Ka-Band Lens Antennas for LEO Satellites," IEEE Trans. Antennas Propag. **56**(5), 1251–1258 (2008).
4. S. Liu, H. Sato, and Q. Chen, "A Wideband, 1 bit Transmitarray Antenna Design With Flat Gain Response," IEEE Trans. Antennas Propag. **68**(10), 7046–7055 (2020).
5. D. M. Pozar, S. D. Targonski, and H. D. Syrigos, "Design of millimeter wave microstrip reflectarrays," IEEE Trans. Antenn. Propag. **45**(2), 287–296 (1997).
6. M. K. Amirhosseini and M. M. Taskhiri, "Matched and wideband flat lens antennas using symmetric graded dielectrics," J. Opt. Soc. Am. A **35**(1), 73–77 (2018).
7. D. Berry, R. Malech, and W. Kennedy, "The reflectarray antenna," IEEE Trans. Antennas Propag. **11**(6), 645–651 (1963).
8. Y. Li and Q. Zhu, "Luneburg lens with extended flat focal surface for electronic scan applications," Opt. Express **24**(7), 7201–7211 (2016).
9. B. Fuchs, O. Lafond, S. Rondineau, and M. Himdi, "Design and characterization of half Maxwell fish-eye lens antennas in millimeter waves," IEEE Trans. Microw. Theory Techn. **54**(6), 2292–2300 (2006).
10. Y. Su and Z. N. Chen, "A Flat Dual-Polarized Transformation-Optics Beamscanning Luneburg Lens Antenna Using PCB-Stacked Gradient Index Metamaterials," IEEE Trans. Antennas Propag. **66**(10), 5088–5097 (2018).
11. B. Arigong, J. Shao, H. Ren, R. Zhou, H. S. Kim, Y. Lin, and H. Zhang, "Flattened generalized luneburg lens via quasi-conformal mapping," in *IEEE Antennas and Propagation Society International Symposium (APSURSI)* (2013), pp. 1902–1903.
12. S. Jain, M. Abdel-Mageed, and R. Mittra, "Flat-lens design using field transformation and its comparison with those based on transformation optics and ray optics," IEEE Antennas Wireless Propag. Lett. **12**, 777–780 (2013).
13. X. Chen, H. F. Ma, X. Y. Zou, W. X. Jiang, and T. J. Cui, "Three-dimensional broadband and high-directivity lens antenna made of metamaterials," J. Appl. Phys. **110**(4), 044904 (2011).
14. J. Bor, B. Fuchs, O. Lafond, and M. Himdi, "Flat foam-based Mikaelian lens antenna for millimeter wave applications," in *44th European Microwave Conference* (2014), pp. 1640–1643.
15. C. Mateo-Segura, A. Dyke, H. Dyke, S. Haq, and Y. Hao, "Flat Luneburg Lens via Transformation Optics for Directive Antenna Applications," IEEE Trans. Antennas Propag. **62**(4), 1945–1953 (2014).
16. A. Mikaelian and A. Prokhorov, "V Self-Focusing Media with Variable Index Of Refraction," Prog. Opt. **17**, 279–345 (1980).
17. J. W. Yang, W. Y. Lai, H. C. Chou, and M. N. M. Kehn, "Compact Mikaelian Lens Synthesized by Metasurfaces," IEEE Antennas Wireless Propag. Lett. **17**(3), 397–400 (2018).

Optics EXPRESS

18. N. García and M. Nieto-Vesperinas, "Left-handed materials do not make a perfect lens," Phys. Rev. Lett. **88**(20), 207403 (2002).
19. C. Gomez-Reino, M. V. Perez, and C. Bao, *Gradient-Index Optics: Fundamentals and Applications*. (Springer, 2002), pp. 128–131.
20. K. Nishizawa, "Principle and application on gradient index optical imaging," Rev. Laser Eng. **8**(5), 748–758 (1980).
21. T. Hayat, M. U. Afzal, A. Lalbakhsh, and K. P. Esselle, "Additively Manufactured Perforated Superstrate to Improve Directive Radiation Characteristics of Electromagnetic Source," IEEE Access **7**, 153445–153452 (2019).
22. M. W. Elsallal, J. Hood, I. McMichael, and T. Busbee, "3D Printed Material Characterization for Complex Phased Arrays and Metamaterials," Microw. J. **59**(10), 20–34 (2016).
23. H. Sato, Y. Takagi, and K. Sawaya, "High Gain Antipodal Fermi Antenna with Low Cross Polarization," IEICE Trans. Commun. **E94-B**(8), 2292–2297 (2011).
24. A. Papathanasopoulos, Y. Rahmat-Samii, N. C. Garcia, and J. D. Chisum, "A novel collapsible flat-layered metamaterial gradient-refractive-index lens antenna," IEEE Trans. Antennas Propag. **68**(3), 1312–1321 (2020).
25. N. C. Garcia and J. D. Chisum, "High-Efficiency, Wideband GRIN Lenses with Intrinsically Matched Unit Cells," IEEE Trans. Antennas Propag. **68**(8), 5965–5977 (2020).
26. M. Imbert, A. Papio, F. De Flaviis, L. Jofre, and J. Romeu, "Design and performance evaluation of a dielectric flat lens antenna for millimeter-wave applications," IEEE Antennas Wireless Propag. Lett. **14**, 342–345 (2015).
27. J. Budhu and Y. Rahmat-Samii, "A novel and systematic approach to inhomogeneous dielectric lens design based on curved ray geometrical optics and particle swarm optimization," IEEE Trans. Antennas Propag. **67**(6), 3657–3669 (2019).
28. J. A. O. Diallo, R. Czarny, B. Loiseaux, and S. Holé, "Comparison Between a Thin Lens Antenna Made of Structured Dielectric Material and Conventional Lens Antennas, in Q-Band in a Compact Volume," IEEE Antennas Wireless Propag. Lett. **17**(2), 307–310 (2018).
29. H. F. Ma, B. G. Cai, T. X. Zhang, Y. Yang, W. X. Jiang, and T. J. Cui, "Three-dimensional gradient-index materials and their applications in microwave lens antennas," IEEE Trans. Antennas Propag. **61**(5), 2561–2569 (2013).
30. M. Liang, W. Ng, K. Chang, K. Gbele, M. E. Gehm, and H. Xin, "A 3-D Luneburg Lens Antenna Fabricated by Polymer Jetting Rapid Prototyping," *IEEE Trans. Antennas Propag*. **62**(4), 1799–1807 (2014).
31. M. R. Dehghani Kodnoeih, Y. Letestu, R. Sauleau, E. Motta Cruz, and A. Doll, "Compact Folded Fresnel Zone Plate Lens Antenna for mm-Wave Communications," IEEE Antennas Wireless Propag. Lett. **17**(5), 873–876 (2018).
32. J. Bor, O. Lafond, H. Merlet, P. L. Bars, and M. Himdi, "Foam based Luneburg lens antenna at 60 GHz," Prog. Electromagn. Res. Lett. **44**, 1–7 (2014).